Available online at www.sciencedirect.com

SciVerse ScienceDirect

journal homepage: www.elsevier.com/locate/he

Interplay between morphology and electrochemical performance of "core–shell" electrocatalysts for oxygen reduction reaction based on a $PtNi_x$ carbon nitride "shell" and a pyrolyzed polyketone nanoball "core"

E. Negro [a,b], S. Polizzi [b,c], K. Vezzù [d], L. Toniolo [b,c], G. Cavinato [a], V. Di Noto [a,b,*]

[a] Department of Chemical Sciences, University of Padova, Via Marzolo 1, I-35131 Padova (PD), Italy
[b] Consorzio Interuniversitario Nazionale per la Scienza e la Tecnologia dei Materiali, INSTM, Italy
[c] Department of Molecular Sciences and Nanosystems – University of Venice, Calle Larga S. Marta, Dorsoduro, 2137-30123 Venezia (VE), Italy
[d] Veneto Nanotech S.C.p.a., Via San Crispino 106, I-35129 Padova (PD), Italy

ARTICLE INFO

Article history:
Received 27 April 2013
Received in revised form
25 July 2013
Accepted 12 August 2013
Available online 14 September 2013

Keywords:
PEM fuel cells
"Core–shell" carbon nitride (CN) electrocatalysts
Oxygen reduction reaction
HR-TEM
CV-TF-RRDE method

ABSTRACT

The interplay between morphology and electrochemical performance of a new class of "core–shell" electrocatalysts for the oxygen reduction reaction (ORR) is studied. The electrocatalysts, labelled PtNi–CN_l T_f/ST_p, consist of a "core" of pyrolyzed polyketone nanoballs (indicated as ST_p "core" support) covered by a carbon nitride (CN) "shell" matrix embedding $PtNi_x$ alloy NPs (indicated as $PtNi_x$-CN). The electrocatalysts are characterized by means of: (a) high-resolution transmission electron microscopy (HR-TEM); and (b) cyclic voltammetry with the thin-film rotating ring-disk electrode (CV-TF-RRDE) method. The structure of the ST_p "core" supports and the details of the preparation procedure, such as pyrolysis temperature, T_f, and treatment with H_2O_2, play a crucial role on modulating: (a) the morphology; and (b) the ORR performance of the electrocatalysts. In particular, the best results are achieved for PtNi–CN_l T_f/ST_p systems: (a) including a ST_p "core" support with a high porosity; and (b) obtained at T_f = 600 °C. It is demonstrated that in general, the treatment with H_2O_2 of electrocatalysts is detrimental for the ORR performance. Nevertheless, in particular conditions, the treatment in H_2O_2 improves the ORR performance of PtNi-CN_l T_f/ST_p. The results presented in this work allow to elucidate the complex correlation existing between: (a) the composition; (b) the interactions in $PtNi_x$-CN; (c) the morphology of ST_p and PtNi–CN_l T_f/ST_p; and (d) the ORR performance of the electrocatalysts.

* *Corresponding author*. Department of Chemical Sciences, University of Padova, Via Marzolo 1, I-35131 Padova (PD), Italy. Tel./fax: +39 (0)49 827 5229.
E-mail address: vito.dinoto@unipd.it (V. Di Noto).

0360-3199/$ – see front matter
http://dx.doi.org/10.1016/j.ijhydene.2013.08.053

1. Introduction

The development of innovative electrocatalysts is one of the most important aspects of the modern research in the field of proton exchange membrane fuel cells (PEMFCs) [1]. This latter breakthrough technology shows great potential to play a major role in a variety of disparate applications, ranging from the electrification of surface transport to the efficient exploitation of the energy derived from renewable sources [2]. However, significant drawbacks are still to be addressed before PEMFCs can be applied commercially on a large scale. In particular, traditional PEMFCs operate at $T < 120$ °C; furthermore, they adopt electrolytes generating a highly acidic environment at the electrodes, e.g., perfluorinated ionomers and sulfonated aromatic polymers [3–5]. In these conditions, the redox process responsible of the operation of PEMFC electrodes require suitable electrocatalysts to achieve a performance level compatible with the applications [6]. In particular, the kinetics of the oxygen reduction reaction (ORR) is very sluggish, and is one of the most important bottlenecks in the overall performance of the PEMFC [6,7]. The best ORR activity in the operating conditions typical of PEMFCs is afforded by active sites based on platinum-group metals such as platinum or palladium [6,8]. The abundance of these elements in the Earth's crust is very limited, giving rise to high costs and a significant risk of supply bottlenecks [9,10]. Despite these shortcomings, as of today the only viable ORR electrocatalysts for application in PEMFCs include active sites based on platinum-group metals [6,8]. In state-of-the-art ORR electrocatalysts, the loading of platinum-group metals is reduced by dispersing the active sites on a conductive support characterized by a large surface area (e.g., XC-72R carbon black nanoparticles) [8,11]. However, there is still a significant need to improve the performance and durability of the electrocatalysts devised following this general approach [1,2,12]. On one hand, the intrinsic turnover frequency of the active sites may be improved above the level showed by systems including only pristine platinum-group metals [1,13]. This result is generally accomplished by alloying the platinum-group metal with a first-row transition metal such as Fe, Co, Ni, Cu and others [13–17]. On the other hand, the durability of the electrocatalysts should be enhanced. In particular: (a) the aggregation of the platinum-group metal nanoparticles bearing the active sites should be prevented; and (b) the degradation of the interfaces between the support and the platinum-group metal nanoparticles should be inhibited [12]. In principle, there is the possibility to achieve the above-described targets by synthesizing the ORR electrocatalysts according to a new procedure developed over the last years [18,19]. This procedure is unique, and is completely different with respect to the well-assessed synthetic procedures reported in the literature [8,11,20]. In summary, the electrocatalysts are obtained by the pyrolysis of a hybrid inorganic-organic precursor, followed by suitable activation processes [18,19]. The proposed procedure is extremely flexible, since it allows to obtain active sites characterized by a well-controlled chemical composition [21–23]. Furthermore, heteroatoms such as nitrogen can be introduced in the electrocatalysts where desired. Thus, graphitic-like carbon nitride-based matrices (CN) are obtained, with N-based ligands coordinating the metal alloy nanoparticles [24]. It was demonstrated that a high concentration of nitrogen in the CN matrix improves the tolerance of the electrocatalyst to the decomposition in oxidizing conditions [25]. Furthermore, significant efforts are still needed to optimize this preparation procedure to yield ORR electrocatalysts improved with respect to the state of the art. Recently, most efforts were devoted to improve the morphology of the electrocatalysts [26,27]. It was proposed that "core–shell" morphologies of CN-based electrocatalysts are of crucial importance to improve the ORR performance and to obtain a high dispersion of the active sites. In the "core–shell" morphology, the carbon nitride (CN) "shell" matrix embedding the metal nanoparticles bearing the active sites is supported on a "core" of conducting nanoparticles [26,27].

In this work, innovative "core" supports based on pyrolyzed polyketone nanoballs are used in the preparation of a family of $PtNi_x$ alloy "core–shell" carbon nitride-based electrocatalysts as described elsewhere [28]. These electrocatalysts present a formula $PtNi–CN_l$ T_f/ST_p, where $PtNi–CN_l$ T_f refers to the "shell", and ST_p denotes the electrolcatalysts' "core". The electrocatalysts' morphology and ORR electrochemistry are investigated extensively by means of HR-TEM and the CV-TF-RRDE method, respectively. The aim of the paper is to achieve a detailed insight of the complex interplay between the electrochemical mechanism and "*ex situ*" performance and the: (a) features of the conducting ST_p "core" supports; (b) parameters of the preparation procedure; (c) morphology of the final electrocatalysts; (d) chemical composition of both the $PtNi_x$-CN "shell" and the ST_p "core" supports; (e) interactions between the CN matrix and the $PtNi_x$ alloy nanoparticles (NPs).

2. Experimental

2.1. Preparation of the $PtNi–CN_l$ T_f/ST_p electrocatalysts

The electrocatalysts investigated in this work are obtained as described elsewhere [28] using a procedure which involves two main steps: (a) preparation of the ST_p "core" supports; and (b) synthesis of the electrocatalysts. The ST_p "core" supports are obtained by growing polyketone (PK) fibers on XC-72R carbon nanoparticles; subsequently, the samples are treated with conc. H_2SO_4 and undergo a series of pyrolysis steps under vacuum. Two ST_p "core" supports are obtained, labelled "S500" and "S700", which are prepared with a pyrolysis step carried out at $T_p = 500$ and 700 °C, respectively. The electrocatalysts are synthesized by impregnating each ST_p "core" support with a PtNi-based Z-IOPE precursor [18,19,26]. These systems undergo a series of pyrolysis steps and suitable treatments to obtain the desired electrocatalysts. The "core–shell" electrocatalysts are labelled as proposed elsewhere [19]: "$PtNi–CN_l$ T_f/ST_p", where "$PtNi–CN_l$" indicates the "shell" consisting of $PtNi_x$ alloy NPs embedded in a CN "shell" matrix, and the "core" is made of conducting ST_p nanoparticles obtained as described above. T_f is the temperature of the pyrolysis process to obtain the electrocatalyst. Four electrocatalysts

are obtained: "PtNi–CN_l 600/S500"; "PtNi–CN_l 900/S500"; "PtNi–CN_l 600/S700"; and "PtNi–CN_l 900/S700". An aliquot of each of these materials is further treated with H_2O_2, 5% vol., yielding four additional systems, which are indexed with the suffix "(w)" and labelled as follows: "PtNi–CN_l 600/S500(w)"; "PtNi–CN_l 900/S500(w)"; "PtNi–CN_l 600/S700(w)"; and "PtNi–CN_l 900/S700(w)".

2.2. *Instruments and methods*

HR-TEM analysis is carried using the experimental setup and the sample preparation techniques described elsewhere [21]. The analysis is executed at 300 kW with a Jeol 3010 apparatus mounting a Gatan slowscan 794 CCD camera. The samples are suspended in isopropyl alcohol; a 5 μL drop of the suspension is deposited on a holey carbon film supported on 3 mm copper grid. The chemical composition of the electrocatalysts is determined by ICP-AES and microanalysis as described in our earlier papers [26,28]. The assay of Pt, Ni and K is determined using the method of standard additions using the following emission lines: λ(Pt) = 214.423 nm; λ(Ni) = 231.604 nm; λ(K) = 766.490 nm. Sample mineralization is carried out by placing a weighed aliquot (~10 mg) of each material in a closed crucible at 600 °C for 3 h in a ventilated oven. The product is dissolved with hot aqua regia and brought to volume in a volumetric flask. The assay of C, H, and N is evaluated using a FISONS EA-1108 instrument. The results are included in Supplementary Data for the sake of completeness. The details of the procedure adopted in the preparation of the electrodes to carry out the electrochemical measurements with the CV-TF-RRDE method are reported elsewhere [21,26]. Briefly, each electrocatalyst is mixed with XC-72R in a 1:1 weight ratio and ground in a mortar, yielding a homogeneous powder. Catalyst inks are prepared by suspending these mixtures in suitable amounts of milli-Q water and a commercial Nafion 1100 solution (Alfa Aesar, 5% weight). The electrode bearing the EC-20 reference electrocatalyst (ElectroChem, 20 wt% Pt on XC-72R), labeled "Pt/C reference", is prepared with the same procedure; the only difference is that no further XC-72R is added. The loading of platinum on the tip of each electrode is equal to 15 μg cm^{-2}. The electrochemical measurements are carried out using a model 636 rotating ring-disk electrode system manufactured by Princeton Applied Research connected to a multi-channel VSP potentiostat/galvanostat produced by BioLogic. The complete descriptions of the experimental setup and of the measurement procedure used to execute the electrochemical investigations reported in this paper are found in the literature [26]. The exact determination of the RHE potential is carried out immediately before each measurement as described elsewhere [6].

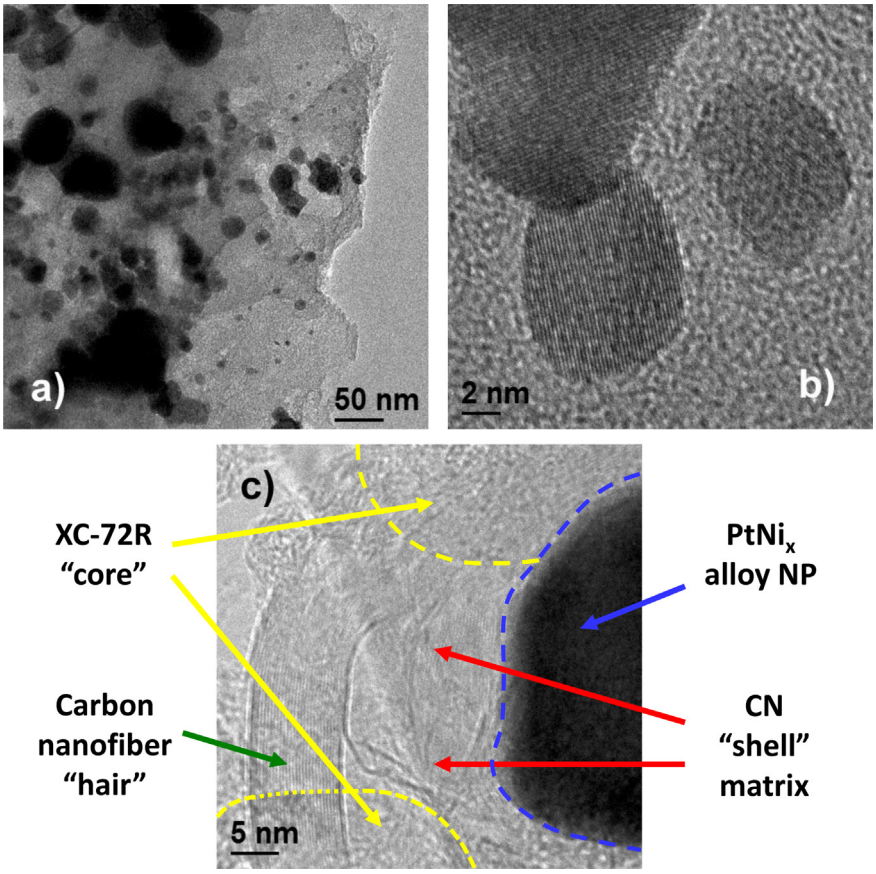

Fig. 1 – HR-TEM micrographs of the electrocatalysts. (a) Overall morphology of PtNi–CN_l 900/S700; (b) $PtNi_x$ alloy NPs embedded in the CN "shell" matrix of PtNi–CN_l 600/S700; and (c) detail of the morphology of the S700 "core" support of PtNi–CN_l 900/S700.

3. Results and discussion

3.1. HR-TEM investigations

The main features of the morphology of the PtNi–CN_l T_f/ST_p electrocatalysts are shown in Fig. 1. Highly polydisperse dark spots associated with $PtNi_x$ alloy NPs are scattered throughout a light matrix (see Fig. 1(a)). The very small $PtNi_x$ alloy NPs present a particle size $d < 10$ nm (see Fig. 1(a and b)), while the large submicrometric NPs show $d > 50$ nm. Fig. 1(c) discloses the morphology of: (a) XC-72R NPs introduced in the first phase of the preparation of the ST_p "core" supports; (b) the pyrolyzed nanofibers of polyketone nanoballs embedding ST_ps; and (c) the CN "shell" matrix supported on the conducting ST_ps. The morphology of the CN matrix is very rough and highly porous (see Fig. 1(c)). Thus, it is expected that the PtNi–CN_l T_f/ST_p electrocatalysts are characterized by a large surface area. The carbon nanofiber "hairs" present on the surface of the ST_ps improve the dispersion of the active electrocatalytic sites present in the $PtNi_x$-CN "shell", as witnessed Fig. 1(c). Fig. 2 shows HR-TEM images of the $PtNi_x$ alloy NPs embedded in the CN "shell" matrix of the electrocatalysts. Well-defined atomic planes are identified in both the $PtNi_x$ alloy NPs (see Fig. 2(a)) and in the $PtNi_x$ alloy submicrometric NPs (see Fig. 2(b)). An interplanar distance of ca. 1.9 Å is determined for both the $PtNi_x$ alloy NPs and the $PtNi_x$ alloy submicrometric NPs (see Fig. 2(a') and (b')), which is consistent with the (002) planes of a $PtNi_x$ alloy nanocrystal characterized by a cubic fcc structure with a cell constant equal to ca. 3.8 Å. With respect to pure Pt crystals, the contraction of the cell constant is consistent with $PtNi_x$ alloy NPs where ca. 40–50% of the lattice sites are occupied by Ni atoms [29–31]. In summary, regardless of their size, the $PtNi_x$ alloy NPs show an x equal to ca. 1. This stoichiometry is corresponding to the metal ratio value determined in the electrocatalysts by ICP-AES (see Supplementary Data). The typical morphology of the ST_p "core" support and the CN "shell" matrix of the PtNi–CN_l T_f/ST_p is revealed in Fig. 3.Fig. 3(a) shows the very rough and highly porous morphology of the CN matrix, while Fig. 3(b) highlights the morphology of carbon nanofibers grown on the S500 "core" support. The HR-TEM images shown in Fig. 3(a and b) disclose that both the CN "shell" matrix and the nanofibers present interplanar distances equal to ca. 3.3 Å, which correspond to the spacing between the (002) planes of graphite-like nanocrystals [32]. The typical modulation of the morphology of the PtNi–CN_l T_f/ST_p electrocatalysts as T_f is raised from 600 to 900 °C is shown in Fig. 4. Fig. 4(a1) and (a2) show that the average size of the $PtNi_x$ alloy submicrometric NPs increases from 70 ± 17 nm for PtNi–CN_l 600/S700 to 136 ± 32 nm for PtNi–CN_l 900/S700. In addition, Fig. 4(b1) and (b2) demonstrate that the average size of the $PtNi_x$ alloy NPs is equal to 8.2 ± 2.1 nm and 10.7 ± 3.5 nm for PtNi–CN_l 600/S500 and PtNi–CN_l 900/S500, respectively. The morphology of S500 and S700 "core" supports used for the preparation of the PtNi–CN_l T_f/ST_p electrocatalysts is consistent with that shown in details elsewhere [28], as follows: (a) both S500 and S700 ST_p "core" supports are characterized by a relatively small

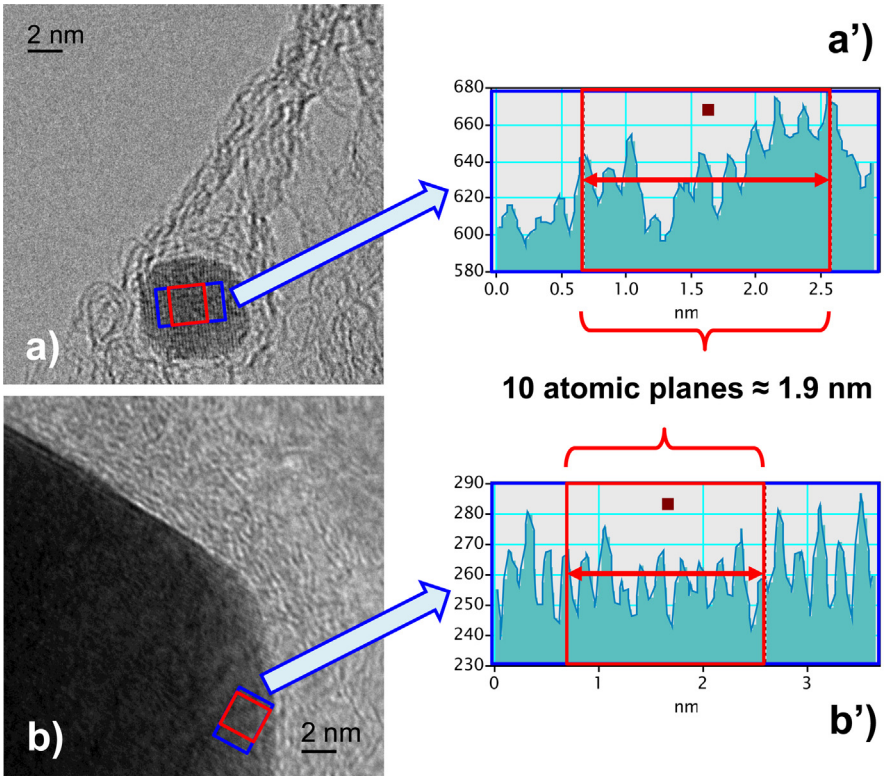

Fig. 2 – Micrographs of the $PtNi_x$ alloy NPs of PtNi–CN_l T_f/ST_p electrocatalysts. (a) $PtNi_x$ alloy NP in PtNi–CN_l 900/S500; and (b) $PtNi_x$ alloy submicrometric NP in PtNi–CN_l 900/S700. (a') and (b') are plots of the interplanar distance in $PtNi_x$ alloy NPs.

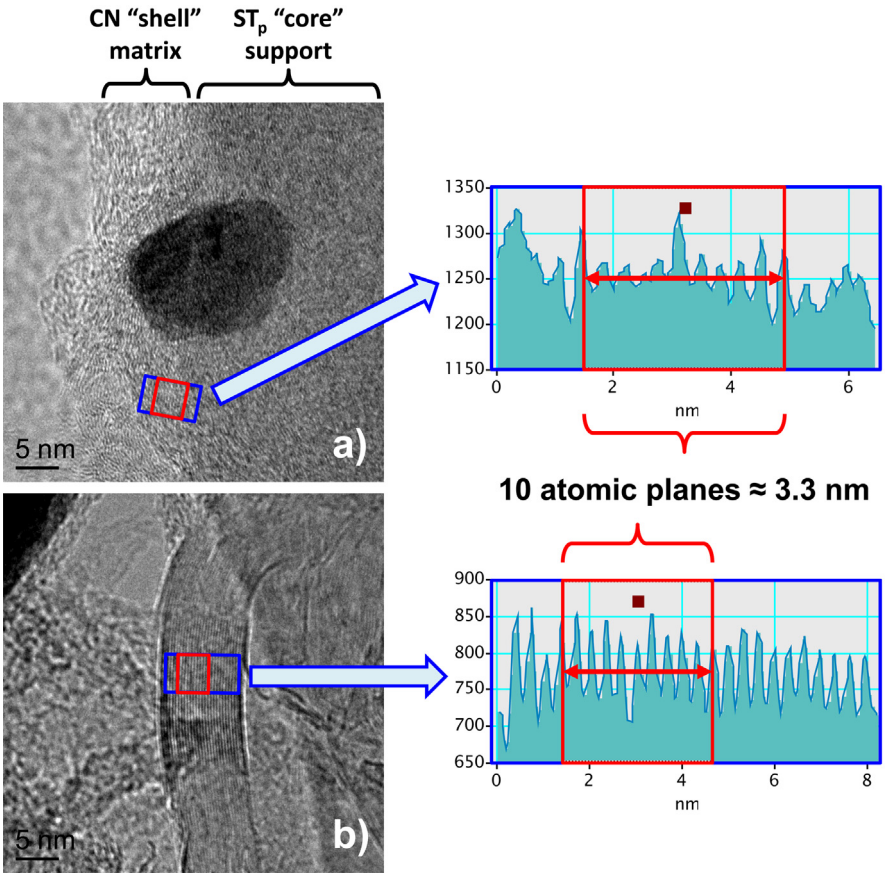

Fig. 3 – Morphology of CN "shell" matrix and ST$_p$ "core" support of the PtNi–CN$_l$ T_f/ST$_p$ electrocatalysts. (a) Nanoporous CN "shell" matrix covering the surface of the S500 "core" support in PtNi–CN$_l$ 600/S500; and (b) carbon nanofiber grown on the surface of carbon NPs in the S700 "core" support of PtNi–CN$_l$ 900/S700.

external surface area, on the order of ca. 60–70 $m^2\ g^{-1}$; (b) most of the surface area of the ST$_p$ "core" supports is originated from the internal micropores (area of the micropores); values of ca. 380 and 215 $m^2\ g^{-1}$ are determined for S500 and S700, respectively; and (c) XC-72R carbon nanoparticles are characterized by the largest external surface area (ca. 105 $m^2\ g^{-1}$) and by the lowest area of the micropores (ca. 80 $m^2\ g^{-1}$). Very small PtNi$_x$ alloy NPs are obtained in the electrocatalyst if the Z-IOPE precursor is spread as a thin layer over a conducting "core" support [27]. If the Z-IOPE precursor does not cover uniformly the "core" support, the metal alloy particles grow to a much larger size since each alloy nucleation site is able to aggregate together metal atoms from a much larger volume of the Z-IOPE precursor during the pyrolysis process [27]. Therefore, the observed morphology of PtNi–CN$_l$ T_f/ST$_p$ electrocatalysts is explained admitting that the Z-IOPE precursor: (a) is covering as a thin layer the large area of the micropores of the ST$_p$ "core" supports; and (b) does not envelop efficiently the external surface of the ST$_p$ "core" supports, owing to their relatively low external surface area. Thus: (a) the PtNi$_x$ alloy NPs are mostly obtained within the internal micropores; and (b) the PtNi$_x$ alloy submicrometric NPs are grown in the "bulk-like" domains of Z-IOPE precursor located on the external surface of the ST$_p$ "core" supports. This model for the interpretation of the morphology of the PtNi–CN$_l$ T_f/ST$_p$ electrocatalysts is depicted in Fig. 5. For the sake of comparison, the PtNi–CN$_l$ 600/G electrocatalyst obtained by impregnating XC-72R carbon NPs with the same Z-IOPE precursor adopted in this work does not embed very large PtNi$_x$ alloy submicrometric particles [27]. This evidence is interpreted admitting that, with respect to S500 and S700 NPs, the surface of XC-72R carbon NPs is covered by the Z-IOPE precursor much more homogeneously. Indeed, the external surface area of XC-72R carbon NPs is significantly larger in comparison with S500 and S700. This scenario accounts of the effect of T_f increasing from 600 to 900 °C (see Fig. 4(a1) and (a2)) on the morphology of the PtNi$_x$ alloy NPs and of the PtNi$_x$ alloy submicrometric NPs. Indeed, the size of PtNi$_x$ alloy NPs is quite independent of T_f, thus confirming that the formation of PtNi$_x$ alloy NPs is promoted by the thermally-activated diffusion of metal atoms originating from the amount of Z-IOPE precursor surrounding the aggregation seed during the pyrolysis process [27]. It is expected that the diffusion and segregation process of the metal atoms are facilitated as T_f is raised. However, the flux of incoming metal atoms towards the aggregation seed depends critically on the "*dimensionality*" of the migration pathways, i.e. on the amount and the porosity of pyrolyzed Z-IOPE precursor.

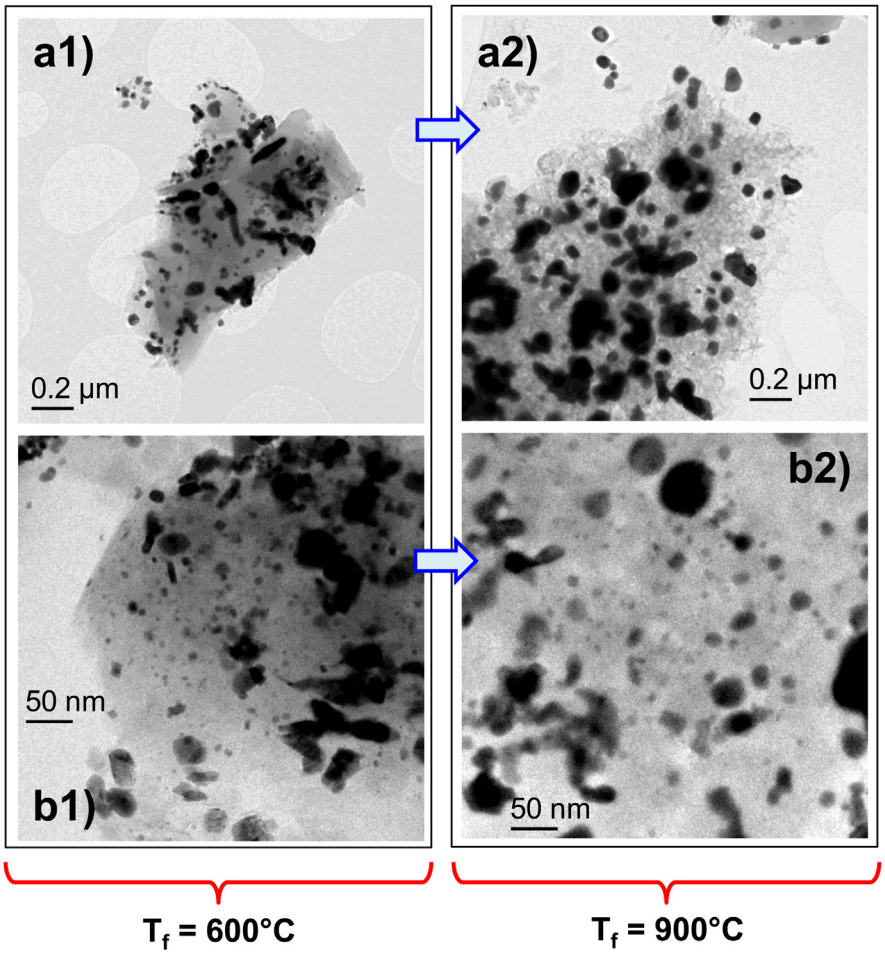

Fig. 4 – Effect of T_f on the morphology of the $PtNi_x$ alloy NPs. Morphology of: $PtNi–CN_l$ 600/S700 (a1); $PtNi–CN_l$ 900/S700 (a2); $PtNi–CN_l$ 600/S500 (b1); and $PtNi–CN_l$ 900/S500 (b2).

Indeed, the pyrolysis of Z-IOPE precursor domains of Type I (see Fig. 5) is able to aggregate a larger amount of metals in a 3D geometry, while in Type II the Z-IOPE precursor thin-layer domains covering the internal surface of the micropores inhibit the growth of $PtNi_x$ alloy NPs. Thus, Type I Z-IOPE precursor domains generate $PtNi_x$ alloy submicrometric NPs, while Type II yields $PtNi_x$ alloy NPs. This hypothesis is schematically described in details in Fig. 6. The effect on the morphology of $PtNi–CN_l$ T_f/ST_p electrocatalysts of the treatment with H_2O_2 is shown in Fig. 7. In general, the treatment with H_2O_2 leads to a significant decrease in the concentration of the $PtNi_x$ alloy NPs (see Fig. 7(a1) and (a2)). Similar results are obtained for $PtNi–CN_l$ 600/S700 and $PtNi–CN_l$ 900/S700 (see Supplementary Data). Nevertheless, as shown in Fig. 7(b1) and (b2), $PtNi–CN_l$ 600/S500 is an exception. These results are interpreted considering that H_2O_2 oxidizes the functional groups present at the interface between the CN matrix and the $PtNi_x$ alloy NPs, facilitating the removal of the metal NPs. With respect to $PtNi_x$ alloy submicrometric NPs, this phenomenon probably affects more significantly $PtNi_x$ alloy NPs which, owing to their small size, are characterized a much higher surface/volume ratio. In the case of $PtNi–CN_l$ 600/S500: (a) the S500 "core" support is very porous, as witnessed by its large area of the micropores; and (b) a relatively high concentration of nitrogen is evidenced in the chemical composition of the material, since $T_f = 600$ °C (see Supplementary Data). In summary, results suggest that in $PtNi–CN_l$ 600/S500: (a) the morphology of the pristine S500 "core" support is not affected significantly by the subsequent pyrolysis processes; S500 maintains the original high porosity; (b) a CN "shell" matrix embedding the $PtNi_x$ alloy NPs is obtained, which exhibits a good adhesion with the S500 "core" support owing to the large area of the micropores of the latter; and (c) the N-based functional groups of the CN "shell" matrix are able to stabilize efficiently the $PtNi_x$ alloy NPs owing to the formation of "coordination nests" [24]. On the other hand, the H_2O_2 treatment of $PtNi–CN_l$ 900/ST_p electrocatalysts reduces significantly the density of $PtNi_x$ alloy NPs owing to the relatively small concentration of N-based functional groups in the CN "shell" matrices. In the case of $PtNi–CN_l$ 600/S700 the porosity of the S700 "core" support is inferior in comparison with S500, as witnessed by the lower area of the micropores. Consequently, the adhesion between the S700 "core" support and the CN "shell" matrix is likely weaker in comparison with $PtNi–CN_l$ 600/S500. The overall outcome is that, with respect to $PtNi–CN_l$ 600/S500,

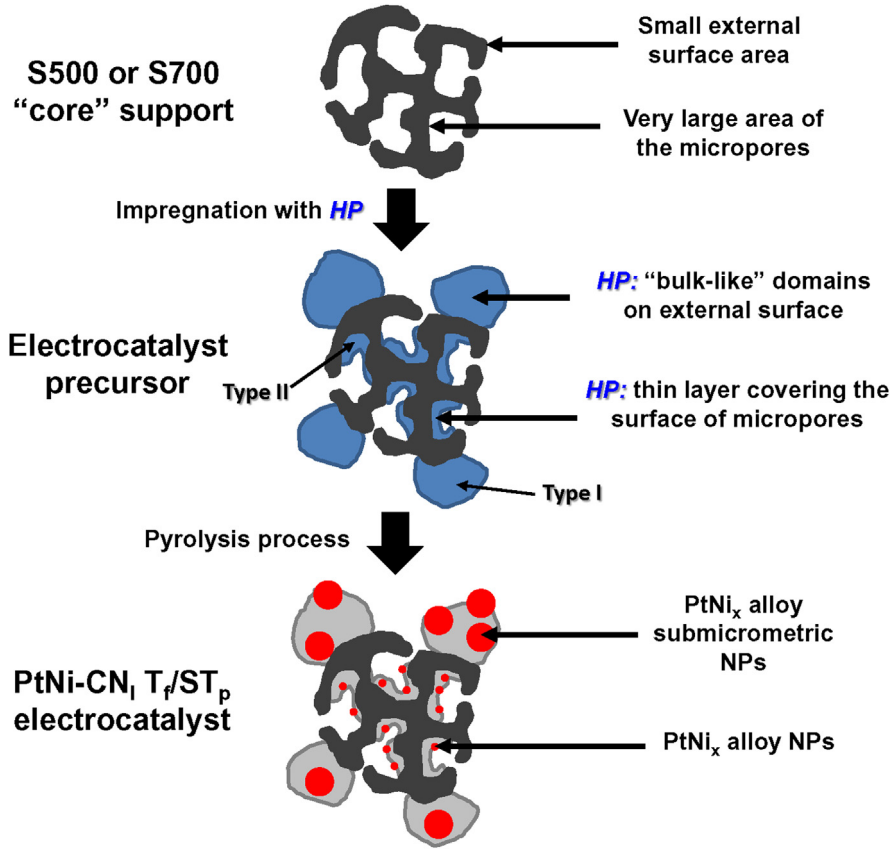

Fig. 5 – Mechanism of pyrolysis and its influence on the morphology of PtNi–CN_l T_f/ST_p electrocatalysts. HP = hybrid inorganic-organic PtNi-based Z-IOPE precursor. S500 and S700 are the conducting "core" supports.

the $PtNi_x$ alloy NPs of PtNi–CN_l 600/S700 are removed more easily during the treatment with H_2O_2.

3.2. . *"Ex situ" investigations of ORR mechanisms and performance*

The CV-TF-RRDE profiles in a pure oxygen atmosphere of the PtNi–CN_l T_f/ST_p pristine electrocatalysts are shown in Fig. 8. Fig. 9 reports the CV-TF-RRDE profiles after treatment with H_2O_2. The results shown in Figs. 8 and 9 for PtNi–CN_l T_f/ST_p and PtNi–CN_l T_f/ST_p(w), respectively, indicate that: (a) the best performance in terms of activation potential and current density is obtained for PtNi–CN_l 600/S500; and (b) in general, the treatment of PtNi–CN_l T_f/ST_p with H_2O_2 increases the ORR overpotential of the electrocatalysts. PtNi–CN_l 600/S500(w) is an exception. Furthermore, to study carefully the ORR mechanism of the proposed electrocatalysts: (a) the current densities and ORR overpotentials determined on the disk electrode are used to evaluate the overall performance of the PtNi–CN_l T_f/ST_p electrocatalysts; while (b) the current measured on the ring electrode is used to measure the ORR selectivity of the electrocatalysts. It is widely accepted that the electrocatalysts are: (a) very selective when the ORR involves a direct 4-electron mechanism yielding water as the final product; and (b) not selective when a large amount of H_2O_2 is formed through a 2-electron mechanism [26,33]. The fraction of H_2O_2 produced by the electrocatalysts in the ORR as a function of the potential is evaluated by means of [34]:

$$X_{H_2O_2} = \frac{\frac{2I_R}{N}}{I_D + \frac{I_R}{N}} \quad (1)$$

where I_D and I_R are the currents detected on the disk and ring electrodes, respectively. $N = 0.38$ is the collection efficiency of the platinum ring. The dependence of $X_{H_2O_2}$ vs. E (see Fig. 10) shows that: (a) both the Pt/C reference and the PtNi–CN_l T_f/ST_p electrocatalysts carry out the ORR towards water almost exclusively with the 4-electron mechanism; and (b) the selectivity of the PtNi–CN_l T_f/ST_p electrocatalysts at $E > 0.25$ V vs. RHE is improved in comparison with the Pt/C reference. This evidence is interpreted considering that the ORR active sites of the PtNi–CN_l T_f/ST_p electrocatalysts include both Pt and Ni atoms [26]. The presence of the Ni atoms promotes the protonation of ORR intermediates, reducing the surface concentration of oxygen-based adsorbates, which are blocking the ORR active sites. A higher surface concentration of free neighbouring Pt coordination sites suitable for O_2 adsorption is thus achieved, which boost the selectivity of the ORR in the 4-electron mechanism [26,27,33]. The behaviour of $X_{H_2O_2}$ profiles is significantly dependent on (a) the morphology of ST_p "core" support (S500 vs. S700); (b) T_f; and (c) the treatment with H_2O_2. In details, the ORR selectivity of the pristine PtNi–CN_l T_f/ST_p electrocatalysts: (a) increases as T_f is raised; and (b) it is

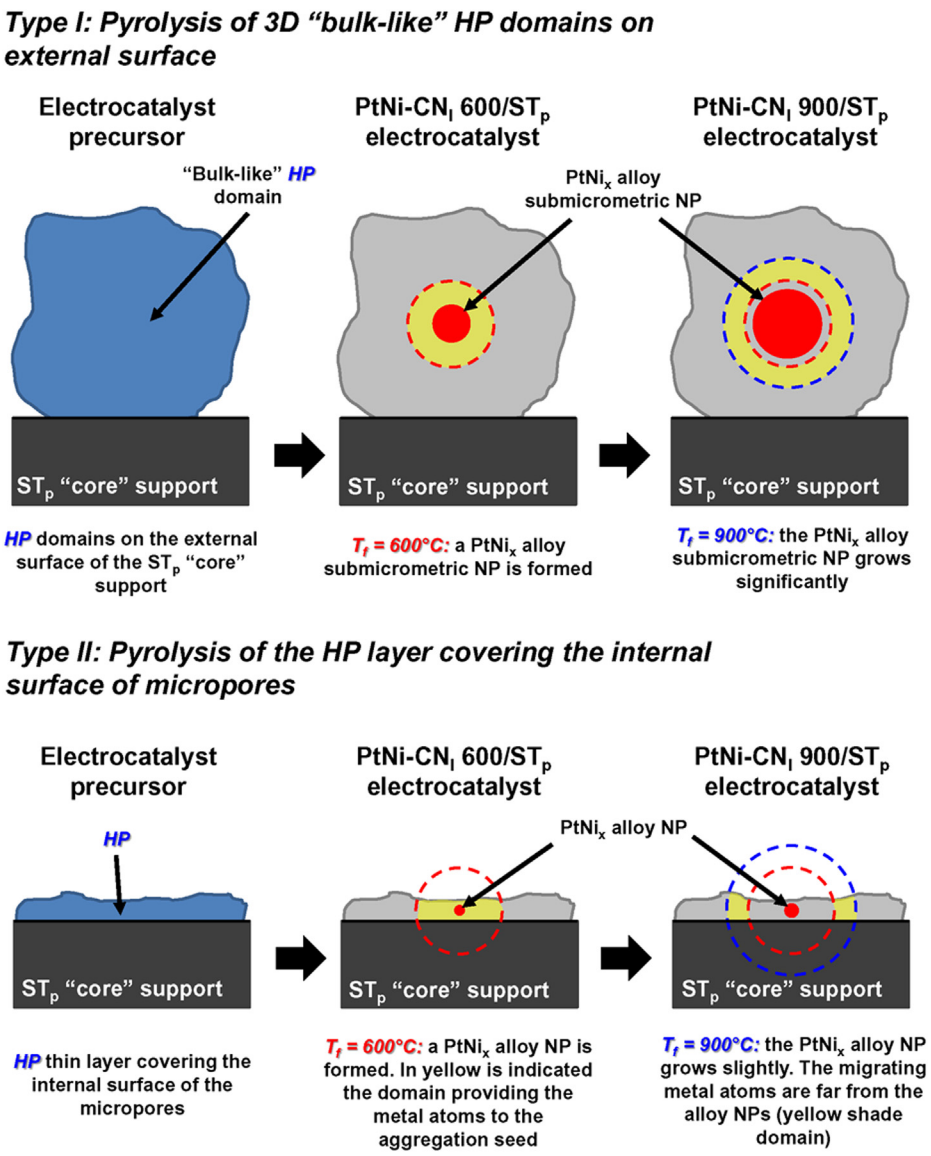

Fig. 6 – Growth mechanisms of $PtNi_x$ alloy submicrometric NPs and $PtNi_x$ alloy NPs.

higher in PtNi–CN_l T_f/S700 in comparison with PtNi–CN_l T_f/S500. These results are rationalized admitting that the coordination of the surface Pt sites by the N-based functional groups present on the CN matrix influences the performance of both the active Pt and the Ni co-catalyst metals. Indeed, it is expected that the ORR selectivity is promoted as the surface concentration of coordinated metal atoms of $PtNi_x$ alloy NPs exposed to reagents is decreased. It should be observed that the Pt and Ni metal atoms in the starting Z-IOPE precursor are in their (II) oxidation state [19,22,35]. During the pyrolysis process, the metal atoms are progressively reduced and coalesced in the $PtNi_x$ alloy NPs bearing on the surface the ORR active sites (see Fig. 1). At the same time, the CN matrix embedding the $PtNi_x$ alloy NPs undergoes oxidation, with a release of volatile species, thus gradually reducing the concentration of coordination ligand functionalities clogging the active sites of $PtNi_x$ alloy NPs. This process is promoted as T_f is increased form 600 to 900 °C, thus explaining the improved ORR selectivity of pristine PtNi–CN_l 900/ST_p electrocatalysts in the 4-electron mechanism in comparison with pristine PtNi–CN_l 600/ST_p. In general, with respect to PtNi–CN_l T_f/S700 samples, the $PtNi_x$ alloy NPs embedded in PtNi–CN_l T_f/S500 are smaller (see Fig. 4) and are characterized by a higher concentration of surface defects such as edge and corner sites, where the coordination of metal atoms by the N-based ligand functionalities provided by the CN "shell" matrix is easier. Correspondingly, a high density of clogged surface metal sites is left behind on the $PtNi_x$ alloy NPs of PtNi–CN_l T_f/S500, leading to a lower selectivity in the 4-electron ORR mechanism. The treatment with H_2O_2 of pristine PtNi–CN_l T_f/S500 increases the ORR selectivity of the resulting PtNi–CN_l T_f/S500(w) (see Fig. 10). Indeed, the H_2O_2 eliminates the N-based ligand functionalities by oxidation, "cleaning" the surface of the $PtNi_x$ alloy NPs, increasing the density of "free" metal active sites. As a result, the surface concentration of couples of free neighbouring Pt sites increases. As expected, the

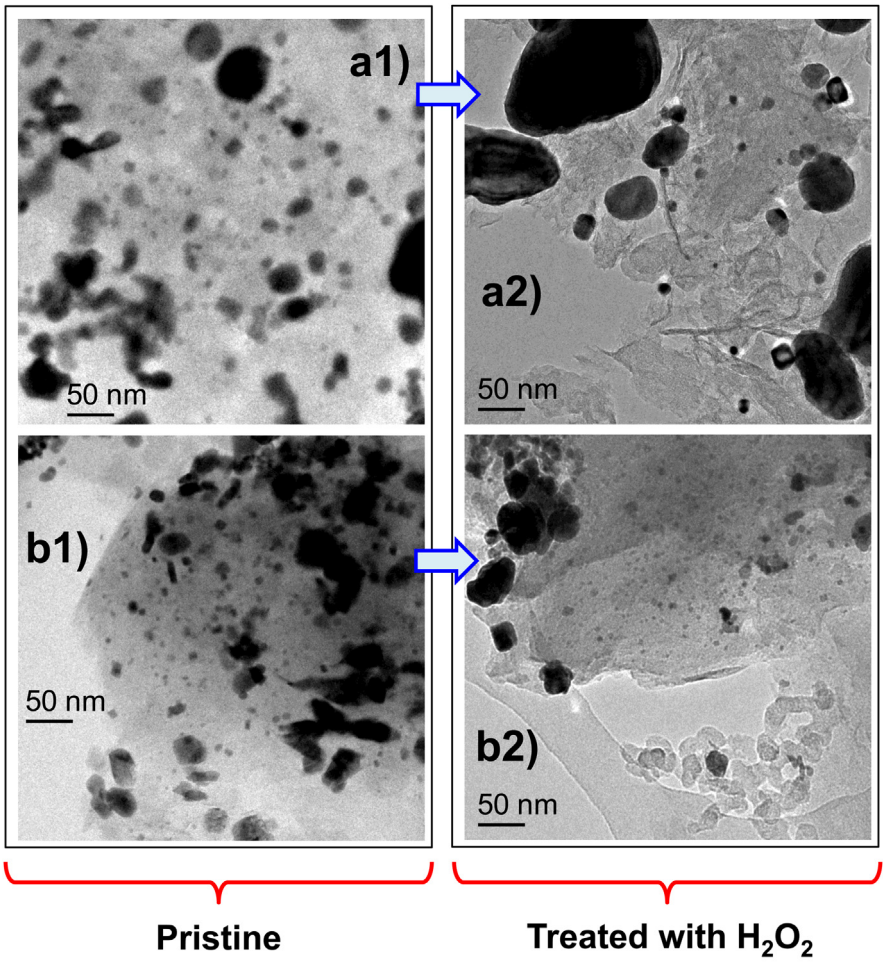

Fig. 7 – Effect of the treatment with H_2O_2 on the morphology of the PtNi–CN_l T_f/ST_p electrocatalysts: (a1) PtNi–CN_l 900/S500; (a2) PtNi–CN_l 900/S500(w); (b1) PtNi–CN_l 600/S500; and (b2) PtNi–CN_l 600/S500(w).

treatment in H_2O_2: a) in the case of PtNi–CN_l 600/S700(w) is not influencing significantly the ORR selectivity; while b) for PtNi–CN_l 900/S700(w) reduces this performance figure (see Fig. 10). This result is easily interpreted considering that the treatment with H_2O_2 reduces the concentration of $PtNi_x$ alloy NPs in PtNi–CN_l T_f/S700 electrocatalysts (see Section 3.2. and Supplementary Data). Indeed, the $PtNi_x$ alloy NPs must be strongly coordinated to the CN matrix to survive to the treatment in H_2O_2. This interpretation accounts of the experimental results obtained from PtNi–CN_l 600/S700, where the CN "shell" matrix includes a significantly higher concentration of nitrogen atoms (see Supplementary Data). Nitrogen-based functionalities provided by the CN matrix are strong coordination ligands for $PtNi_x$ alloy NPs, giving so rise to "coordination nests" which stabilize and activate the active metal NPs [24]. Thus, fewer nitrogen-based ligand functionalities are needed in order to keep fixed in the CN matrix the $PtNi_x$ alloy NPs during the treatment in H_2O_2. In summary, in PtNi–CN_l 600/S700 two phenomena are occurring simultaneously upon the treatment in H_2O_2: a) the N-based ligands are oxidized, improving the ORR selectivity of the $PtNi_x$ alloy NPs; and b) the N-based ligands are required to hinder the elimination of the $PtNi_x$ alloy NPs bearing the $PtNi_x$ ORR active sites. Thus, a compromise between these two phenomena is necessary in order to obtain electrocatalysts with a high performance and selectivity. Indeed, $PtNi_x$ alloy NPs coordinated by a larger concentration of N-based ligands present a lower ORR selectivity and are not eliminated from the CN matrix after the treatment in H_2O_2. In PtNi–CN_l 600/S700 it seems that these two opposite phenomena tend to cancel one another. Indeed, the overall surface concentration of N-based ligand functionalities coordinating $PtNi_x$ alloy NPs does not change significantly during the treatment in H_2O_2, hardly affecting the ORR selectivity of PtNi–CN_l 600/S700(w).

The electrochemical surface area (ECSA) of the $PtNi_x$ ORR active sites of the PtNi–CN_l T_f/ST_p electrocatalysts is determined as described elsewhere [36–38], normalizing the CO stripping charge to the value of 484 μC cm_{Pt}^{-2} [36,39]. The results are reported in Table 1. The values of ESCA reported in Table 1 are consistent with the results obtained from the morphological investigation of PtNi–CN_l T_f/ST_p and discussed in Section 3.2. In particular, the ESCA values of the pristine PtNi–CN_l T_f/ST_p electrocatalysts are significantly lower in comparison with the Pt/C reference. This evidence is

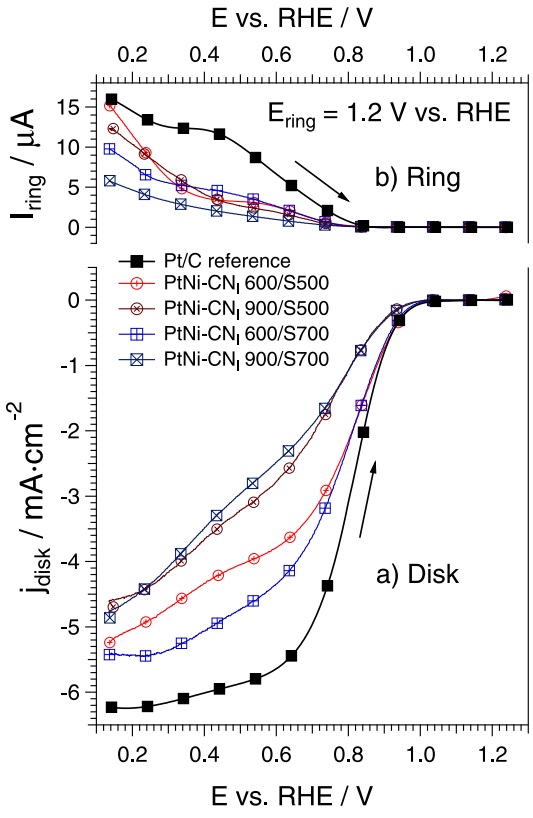

Fig. 8 – Positive-going sweeps of the Pt/C reference and of PtNi–CN$_l$ T_f/ST$_p$ electrocatalysts in a pure O_2 atmosphere. (a) Current densities measured on the glassy-carbon disk; (b) oxidation currents determined on the platinum ring. Cell filled with a 0.1 M $HClO_4$ solution, T = 60 °C, sweep rate = 5 mV s^{-1}, electrode rotation rate 1600 rpm and P_{O_2} = 1 atm.

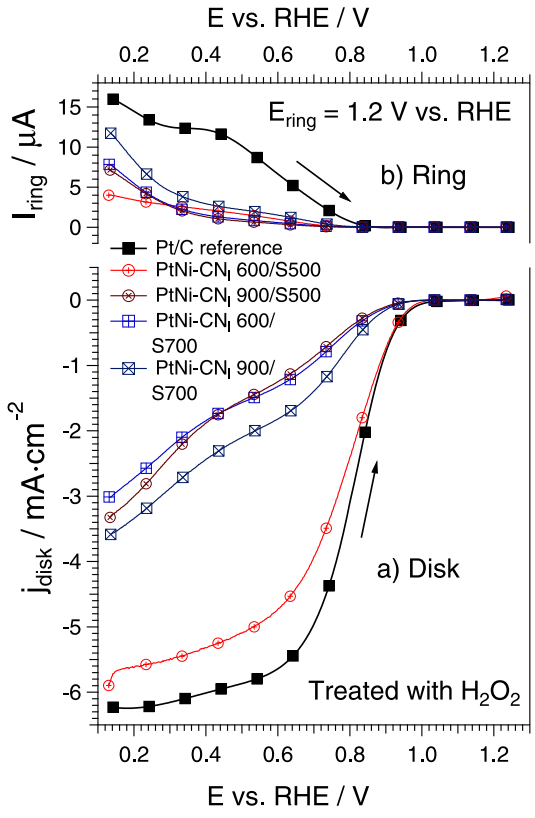

Fig. 9 – Positive-going sweeps of the Pt/C reference and of the PtNi–CN$_l$ T_f/ST$_p$(w) electrocatalysts in a pure O_2 atmosphere. The experimental parameters are reported in the caption of Fig. 8.

interpreted as follows: (a) the wt% of Pt is roughly comparable (within a factor of ca. 2) in the Pt/C reference and in the pristine PtNi–CN$_l$ T_f/ST$_p$ electrocatalysts; (b) PtNi–CN$_l$ T_f/ST$_p$ electrocatalysts include both PtNi$_x$ alloy NPs and PtNi$_x$ alloy submicrometric NPs (see Figs. 1, 2, 4 and 7). The latter, which are characterized by a significantly lower specific surface area, likely aggregate most of the Pt content of the PtNi–CN$_l$ T_f/ST$_p$ electrocatalysts. In general, the treatment of the PtNi–CN$_l$ T_f/ST$_p$ electrocatalysts with H_2O_2 lowers drastically the ESCA. PtNi-CN$_l$ 600/S500 is an exception, since upon treatment in H_2O_2 its ESCA increases from 11.0 to 14.5 m^2 g_{Pt}^{-1} (see Table 1), thus achieving the best performance. These evidences are in accordance with the observed removal of PtNi$_x$ alloy NPs embedded in the CN "shell" matrix of pristine materials upon treatment with H_2O_2. Indeed, this phenomenon is observed for all the PtNi–CN$_l$ T_f/ST$_p$ electrocatalysts except PtNi–CN$_l$ 600/S500 (see Fig. 7 and Supplementary Data). The increase in the ESCA of the latter is interpreted admitting that the treatment in H_2O_2 does not affect significantly the concentration of PtNi$_x$ alloy NPs and that the oxidation of the excess of N-based ligands opens new mass transport pathways in its CN matrix. Consequently, additional PtNi$_x$ ORR active sites, buried deep within the micropores of the support of PtNi–CN$_l$ 600/S500, become available for the ORR in PtNi–CN$_l$ 600/S500(w). To evaluate quantitatively the ORR performance, the contributions arising from the mass transport are removed from the disk current densities j shown in Figs. 8 and 9. Equation 2 is used to determine the faradic ORR current density j_k [6,40]:

$$\frac{1}{j} = \frac{1}{j_k} + \frac{1}{j_d} \tag{2}$$

In this paper, for each electrocatalyst j_d was set equal to the value of the corresponding ORR trace shown in Fig. 8 or Fig. 9 at a potential equal to 0.140 V vs. RHE. The faradic current density j_k obtained from Equation 2 is multiplied by the geometric area of the glassy carbon disk (A = 0.196 cm^2) to obtain the faradic ORR current i_k. i_k is normalized either: (a) on the total mass of Pt of the electrocatalyst deposited on each electrode (ca. 2.95 μg); or (b) on the total Pt surface area on the electrode; this figure is equal to the ESCA values reported on Table 1 multiplied by the total mass of Pt of the catalyst present on the electrode. The resulting two figures of merit are the mass activity i_m and the surface activity i_s [6]. Results of PtNi–CN$_l$ T_f/ST$_p$ and PtNi–CN$_l$ T_f/ST$_p$(w) electrocatalysts are plotted in a semilogarithmic scale ("Tafel plots") on Fig. 11 and Fig. 12, respectively. The performance of the PtNi–CN$_l$ T_f/ST$_p$ electrocatalysts in the ORR is evaluated measuring the values of i_m and i_s at 0.9 V vs. RHE (see Table 1). The main parameter affecting the $i_{m(0.9\ V)}$ values of the pristine PtNi–CN$_l$ T_f/ST$_p$

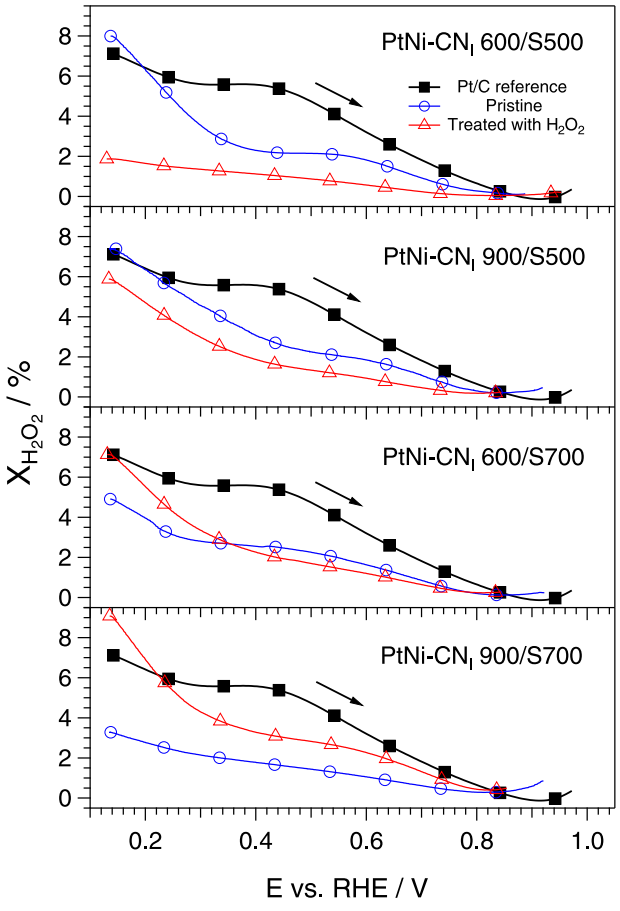

Fig. 10 – Fraction of hydrogen peroxide ($X_{H_2O_2}$) developed during the ORR on the PtNi–CN$_l$ T_f/ST$_p$ electrocatalysts as a function of the potential. ($X_{H_2O_2}$) is determined with Equation (1) from the profiles shown in Figs. 8 and 9.

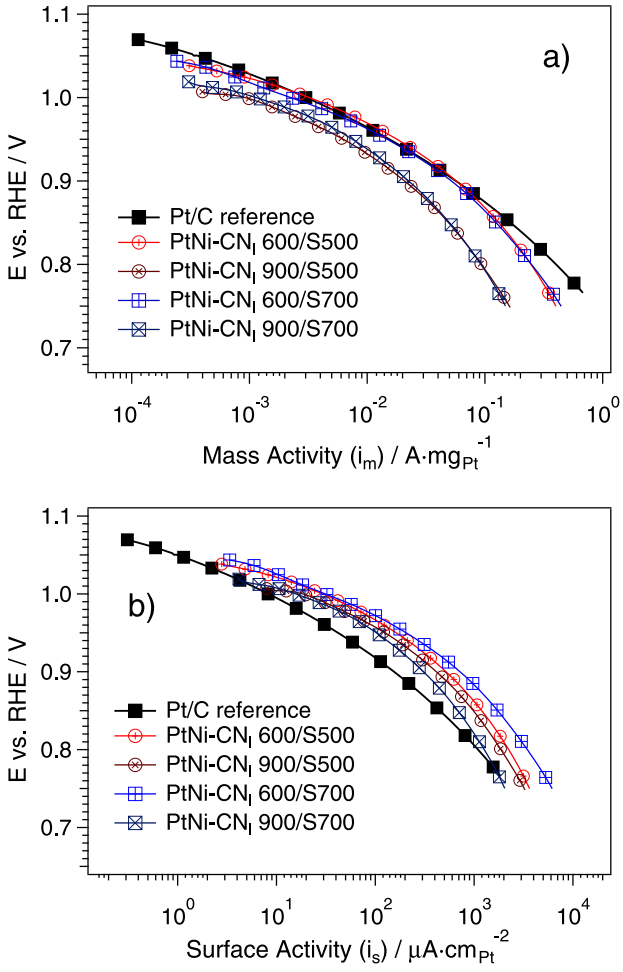

Fig. 11 – Tafel plots of the pristine PtNi–CN$_l$ T_f/ST$_p$ electrocatalysts and of the Pt/C reference. Profiles obtained starting from the traces reported in Fig. 8 after removing the contributions arising from mass transport phenomena. Currents normalized: (a) on the mass of Pt on the electrode; (b) on the ECSA of the active sites evaluated from CO stripping measurements.

electrocatalysts is T_f. The values of $i_{m(0.9\ V)}$ determined on PtNi–CN$_l$ 600/S500 and PtNi–CN$_l$ 600/S700 are very close to that of the Pt/C reference. As T_f is raised from 600 to 900 °C, the values of $i_{m(0.9\ V)}$ are decreased by a factor of ca. 2. This behaviour is interpreted taking into consideration the tendency of the PtNi$_x$ alloy NPs to grow as T_f is raised, thus decreasing the surface area of the ORR active sites. The i_m values of the PtNi–CN$_l$ T_f/ST$_p$ electrocatalysts decrease significantly upon treatment with H_2O_2. This result is ascribed to the dramatic drop in the active surface area of the PtNi$_x$ alloy NPs triggered by the elimination of a significant fraction of the alloy NPs (see Fig. 7 and Supplementary Data). PtNi–CN$_l$ 600/S500 is an exception: its $i_{m(0.9\ V)}$ values are hardly affected by the treatment in H_2O_2, consistently with the survival of the starting concentration of PtNi$_x$ alloy NPs (see Fig. 7). $i_{m(0.9\ V)}$ is a very important figure of merit to gauge the performance of ORR electrocatalysts for practical applications. Indeed, it provides information on the mass of platinum to include in the cathode electrode of a fuel cell running in operative conditions. On the other hand, $i_{s(0.9\ V)}$ is more relevant for the fundamental study of the ORR kinetics on electrocatalysts. The normalization on the Pt surface area allows to estimate the turnover frequency of the active sites of the materials in the ORR [6]. The inspection of Table 1 highlights that the PtNi–CN$_l$ T_f/ST$_p$ electrocatalysts, both pristine and after

Table 1 – Figures of merit of the ORR performance of the proposed electrocatalysts.

Electrocatalyst	ECSA$_{Pt}$/ m^2 g$_{Pt}^{-1}$	$i_{m(0.9\ V)}$/ A mg$_{Pt}^{-1}$	$i_{s(0.9\ V)}$/ μA cm$_{Pt}^{-2}$
PtNi–CN$_l$ 600/S500	11.0	0.057	520
PtNi–CN$_l$ 600/S500(w)	14.5	0.056	385
PtNi–CN$_l$ 900/S500	5.0	0.0208	420
PtNi–CN$_l$ 900/S500(w)	1.2	0.0068	570
PtNi–CN$_l$ 600/S700	7.2	0.052	717
PtNi–CN$_l$ 600/S700(w)	1.9	0.0082	450
PtNi–CN$_l$ 900/S700	7.3	0.0225	306
PtNi–CN$_l$ 900/S700(w)	1.4	0.0105	750
Pt/C reference	36.6	0.0563	153

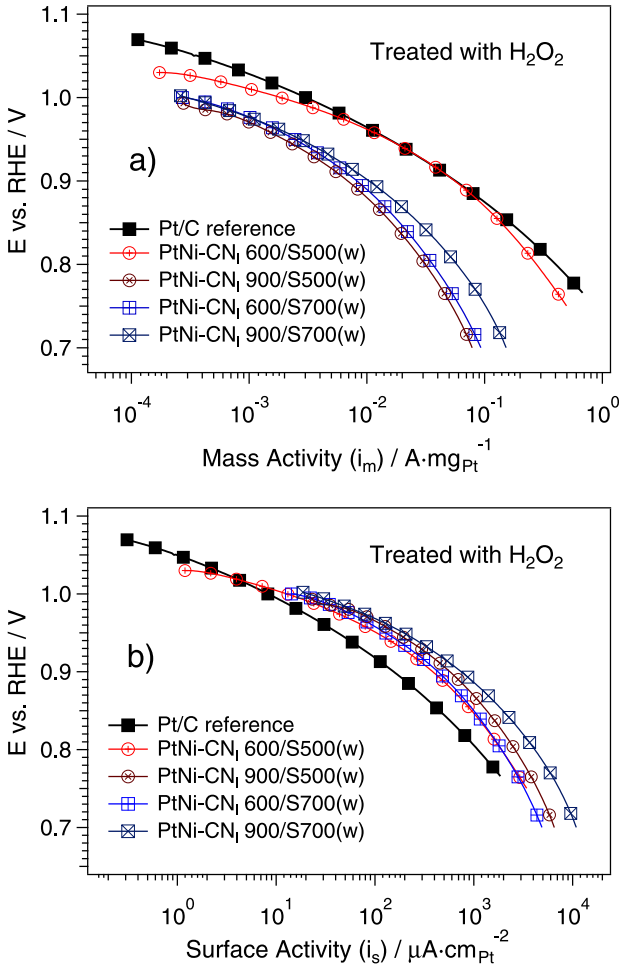

Fig. 12 – Tafel plots of the PtNi–CN$_l$ T_f/ST$_p$(w) electrocatalysts and of the Pt/C reference. Profiles obtained starting from the traces reported in Fig. 9 after removing the contributions arising from mass transport phenomena. Currents normalized: (a) on the mass of Pt on the electrode; (b) on the ECSA of the active sites evaluated from CO stripping measurements.

treatment in H_2O_2, are characterized by a much higher $i_{s(0.9\ V)}$ in comparison with the Pt/C reference. This evidence confirms the results obtained previously by our group for electrocatalysts based on other CN matrices including bimetallic active sites based on platinum and nickel [22,26,35]. The higher turnover frequency is interpreted admitting that the presence of nickel and nitrogen-based ligands of the CN matrix improves the performance of platinum active sites by promoting the rate and density of protonation processes of the ORR intermediates; thus, H_2O is obtained directly, which is immediately desorbed from the Pt active sites [19,26,27]. In summary, Pt active sites are regenerated faster after the reduction of O_2 and are allowed to perform a higher number of $O_2 \rightarrow H_2O$ direct processes in the same span of time. In addition to this "bifunctional" mechanism, the alloying of Pt with Ni is expected to promote the ORR kinetics by means of an "electronic" mechanism. This latter phenomenon is originated by the contraction of the crystallographic cell constant in PtNi$_x$ alloy NPs in comparison with pure Pt nanocrystals (see Fig. 2), which lowers the center of the d-band of the PtNi$_x$ alloy NPs. Thus, the interactions between each ORR active site and the ORR intermediates are weakened [41,42]. Table 1 shows that $i_{s(0.9\ V)}$ of the PtNi–CN$_l$ T_f/ST$_p$ electrocatalysts: (a) for pristine samples, is decreased as T_f is raised; and (b) upon treatment in H_2O_2, it decreases for PtNi–CN$_l$ 600/ST$_p$(w) and increases for PtNi–CN$_l$ 900/ST$_p$(w). This behaviour is interpreted on the basis of the effect of T_f and of the treatment with H_2O_2 on the chemical composition of the ORR active sites. For pristine PtNi–CN$_l$ T_f/ST$_p$ electrocatalysts, $i_{s(0.9\ V)}$ is decreasing as T_f is raised from 600 to 900 °C since the nitrogen-based ligands are coordinated strongly to Pt sites on the surface of the PtNi$_x$ alloy NPs, thus partially blocking the ORR active metals. However, as PtNi–CN$_l$ 900/ST$_p$ are treated with H_2O_2, two phenomena are probably occurring: (a) a significant fraction of the nitrogen-based functional groups are removed (see Supplementary Data); and (b) the alloying of Pt with Ni is more pronounced in comparison with PtNi–CN$_l$ 600/ST$_p$ [22]. Consequently, the nitrogen-based functional groups blocking the active sites are mostly removed, while the improved alloying of Pt with Ni gives rise to a higher contraction of the crystallographic cell of PtNi$_x$ alloy NPs [31]. Thus, the ORR kinetics is promoted by means of an "electronic" mechanism [41,42]. In the case of PtNi–CN$_l$ 600/ST$_p$, the nitrogen-based functionalities of CN matrix are coordinating weakly the Pt active sites, promoting the ORR kinetics by means of a "bifunctional" mechanism described above [19]. However, as the PtNi–CN$_l$ 600/ST$_p$ electrocatalysts are treated in H_2O_2, a fraction of these nitrogen-based coordination ligands of the CN matrix is probably removed, thus inhibiting the "bifunctional" mechanism and reducing $i_{s(0.9\ V)}$. With respect to PtNi–CN$_l$ 600/S500, this latter effect is more evident for PtNi–CN$_l$ 600/S700, in accordance with the more marked decrease in the concentration of nitrogen upon treatment in H_2O_2 (see Supplementary Data). The data reported in Figs. 11 and 12 witness that in the investigated potential range i.e., at E larger than ca. 0.75 V vs. RHE, all the PtNi–CN$_l$ T_f/ST$_p$ electrocatalysts and the Pt/C reference show a very similar trend. Thus, it is expected that these materials carry out the ORR with a very similar mechanism. At E lower than ca. 0.9 V vs. RHE, the Tafel slopes are equal to ca. 120 mV dec^{-1}, which are typical values of the ORR carried out with the 4-electron mechanism on a Pt-based active site where the incoming O_2 molecules can be adsorbed easily [7,33]. As the potential is raised, the Tafel slopes become smaller. This phenomenon suggests that in these conditions the ORR is carried out with the 4-electron mechanism in active sites becoming progressively more clogged with oxygen-based ligand adsorbates. Thus, in this condition the adsorption of the incoming O_2 molecules is hindered [7,19,26,33]. At E higher than ca. 1 V vs. RHE the PtNi–CN$_l$ T_f/ST$_p$ electrocatalysts show Tafel slopes which are significantly lower in comparison with the Pt/C reference, ca. 40 mV dec^{-1} *vs.* ca. 65 mV dec^{-1} of the Pt/C reference, confirming that in comparison with the Pt/C reference: a) as the ORR kinetics of the PtNi–CN$_l$ T_f/ST$_p$ electrocatalysts is improved (see Table 1), the desorption of the ORR intermediates is easier; and b) the adsorption of additional incoming O_2 molecules on the active sites is facilitated and can take place at a higher coverage of oxygen-based

adsorbates. As a result, the Tafel slope is lowered. This effect is particularly pronounced in electrocatalysts such as PtNi–CN_l 600/S500, PtNi–CN_l 600/S500(w) and PtNi–CN_l 600/S700, where the effect of the bifunctional mechanism in ORR kinetics results more relevant. This evidence prompts us to admit that the nitrogen-based functional groups of CN matrix coordinating weakly the bimetallic Pt-based ORR active sites play a crucial role in the modulation of the ORR kinetics, especially at the higher potentials.

4. Conclusions

In this paper, a family of innovative "core–shell" PtNi–CN_l T_f/ST_p electrocatalysts prepared as described elsewhere [28] is extensively investigated to elucidate the interplay between the morphology, the preparation parameters, and the electrochemical performance as determined by the CV-TF-RRDE "*ex situ*" method. The PtNi–CN_l T_f/ST_p electrocatalysts include a very rough and porous CN matrix "shell", derived by the pyrolysis of both the ST_p "core" supports and the supported fraction of the PtNi-based Z-IOPE precursor added during the preparation procedure [22,27]. The PtNi–CN_l T_f/ST_p electrocatalysts embed $PtNi_x$ alloy NPs in the CN "shell" matrix. HR-TEM investigations highlight that two main families of $PtNi_x$ alloy NPs are embedded in the CN "shell" matrix of PtNi–CN_l T_f/ST_p electrocatalysts: (a) $PtNi_x$ alloy NPs, with $d \sim 10$ nm, which likely provide the largest contribution to the ORR activity owing to their large specific area; and (b) $PtNi_x$ alloy submicrometric NPs, with $d > 50$ nm, which probably act to decrease the density of the active sites. These two types of NPs are originated owing to a replica process form the morphology of the ST_p "core" supports as follows. The pyrolysis process of: (a) Z-IOPE precursor domains of Type I on the external surface of ST_p "core" supports yields $PtNi_x$ alloy submicrometric NPs; (b) Z-IOPE domains of Type II covering as a thin layer the internal micropores of the ST_p "core" supports originates $PtNi_x$ alloy NPs. The treatment of PtNi–CN_l T_f/ST_p in H_2O_2 removes most of the $PtNi_x$ alloy NPs; the only exception is PtNi–CN_l 600/S500, owing to: (a) the large surface of the micropores of the S500 "core" support; and (b) the relatively high concentration of nitrogen-based functional ligands of the CN "shell" matrix, which form "coordination nests" [24] able to stabilize effectively the $PtNi_x$ alloy NPs. The ORR performance and selectivity in the 4-electron mechanism of the PtNi–CN_l T_f/ST_p electrocatalysts is heavily influenced by the morphology of the $PtNi_x$ alloy NPs and their chemical interactions with the CN matrix. The ORR selectivity in the 4-electron mechanism is improved: (I) for larger $PtNi_x$ alloy NPs (e.g., in pristine PtNi–CN_l 900/S700); or (II) where the treatment in H_2O_2 removes most of the loosely-bound N-based ligands of CN matrix (e.g., in PtNi–CN_l 600/S500(w)). However, in the former case relatively low ORR currents are registered due to the low total number of available active sites (see Figs. 8 and 9). A high concentration of small $PtNi_x$ alloy NPs results in CV-TF-RRDE curves similar to that of the Pt/C reference. Typical examples are the PtNi–CN_l 600/ST_p and PtNi–CN_l 600/S500(w). The ORR performance is inferior in the cases where: (a) the $PtNi_x$ alloy NPs are characterized by a larger size, e.g., in pristine PtNi–CN_l 900/ST_p; and (b) most of the $PtNi_x$ alloy NPs are removed by treatment in H_2O_2, e.g., in PtNi–CN_l 900/S500(w), PtNi–CN_l 600/S700(w) and PtNi–CN_l 900/S700(w). Taking all together, the intrinsic ORR activity of the PtNi–CN_l T_f/ST_p electrocatalysts is significantly improved, by a factor of ca. 2–5, in comparison with the Pt/C reference as a result of: (a) the alloying of Pt with the Ni atoms in $PtNi_x$ alloy NPs ("electronic mechanism" [41,42]) and (b) the weak coordination of Pt by nitrogen-based ligand functionalities of the CN matrix, ("bifunctional mechanism" [19,26]). In the high-potential regime, at $E > 0.75$ V vs. RHE, the PtNi–CN_l T_f/ST_p electrocatalysts and the Pt/C reference carry out the ORR according to a very similar mechanism. At the highest potentials, i.e., at E higher than ca. 1 V vs. RHE, the adsorption of incoming O_2 molecules in active sites is facilitated. Indeed, in this condition the nitrogen-based ligands of CN matrix weakly coordinating the bimetallic Pt-based active ORR sites lead to lower values of Tafel slopes (ca. 40 mV dec^{-1} *vs.* ca. 65 mV dec^{-1} of the Pt/C reference). Results above summarized give strong evidence that the morphology of the ST_p "core" supports plays a crucial role in the modulation of the morphology of the final electrocatalysts in a very efficient replica phenomenon ("*Qualis pater, talis filius*"). Indeed, the chemical composition of the CN "shell" matrix and its interactions with the $PtNi_x$ alloy NPs affect significantly a number of fundamental features of the PtNi–CN_l T_f/ST_p electrocatalysts, including: (a) the outcome of the treatment in H_2O_2 on the morphology; and (b) the ORR mechanism, selectivity and intrinsic activity. In conclusion, this work provides crucial insight to better exploit the superior flexibility of the proposed preparation route of ST_p "core" supports in the design of new and improved ORR electrocatalysts for application in PEMFCs.

Acknowledgements

This research is funded by project "PRAT 2011" financed by the University of Padova, and by the Italian MURST project PRIN2008 Prot. 2008SXASBC_002. E. Negro thanks Regione del Veneto (SMUPR n. 4148, Polo di ricerca del settore fotovoltaico) for financial support.

Appendix A. Supplementary data

Supplementary data related to this article can be found at http://dx.doi.org/10.1016/j.ijhydene.2013.08.053.

REFERENCES

[1] Gasteiger HA, Markovic NM. Just a dream or future reality? Science 2009;324:48–9.
[2] Wang Y, Chen KS, Mishler J, Cho SC, Adroher XC. A review of polymer electrolyte membrane fuel cells: technology, applications, and needs on fundamental research. Appl Energy 2011;88:981–1007.
[3] Di Noto V, Zawodzinski TA, Herring AM, Giffin GA, Negro E, Lavina S. Polymer electrolytes for a hydrogen economy. Int J Hydrogen Energy 2012;37:6120–31.

[4] Srinivasan S. Fuel cells – from fundamentals to applications. New York: Springer Science; 2006.
[5] Spiegel CS. Designing and building fuel cells. New York: McGraw-Hill; 2007.
[6] Gasteiger HA, Kocha SS, Sompalli B, Wagner FT. Activity benchmarks and requirements for Pt, Pt-alloy, and non-Pt oxygen reduction catalysts for PEMFCs. Appl Catal B-Environ 2005;56:9–35.
[7] Wang JX, Uribe FA, Springer TE, Zhang J, Adzic RR. Intrinsic kinetic equation for oxygen reduction reaction in acidic media: the double Tafel slope and fuel cell applications. Faraday Discuss 2008;140:347–62.
[8] Watanabe M, Tryk DA, Wakisaka M, Yano H, Uchida H. Overview of recent developments in oxygen reduction electrocatalysis. Electrochim Acta 2012;84:187–201.
[9] Appleby AJ. Electrochemical engine for vehicles. Sci Am 1999;281:74–9.
[10] Swart P, Dewulf J. Quantifying the impacts of primary metal resource use in life cycle assessment based on recent mining data. Resour Conserv Recycling 2013;73:180–7.
[11] Morozan A, Jousselme B, Palacin S. Low-platinum and platinum-free catalysts for the oxygen reduction reaction at fuel cell cathodes. Energy Environ Sci 2011;4:1238–54.
[12] Borup R, Meyers J, Pivovar B, Kim YS, Mukundan R, Garland N, et al. Scientific aspects of polymer electrolyte fuel cell durability and degradation. Chem Rev 2007;107:3904–51.
[13] Greeley J, Stephens IEL, Bondarenko AS, Johansson TP, Hansen HA, Jaramillo TF, et al. Alloys of platinum and early transition metals as oxygen reduction electrocatalysts. Nat Chem 2009;1:552–6.
[14] Aricó A, Stassi A, Gatto I, Monforte G, Passalacqua E, Antonucci V. Surface properties of Pt and PtCo electrocatalysts and their influence on the performance and degradation of high-temperature polymer electrolyte fuel cells. J Phys Chem C 2010;114:15823–36.
[15] Stassi A, Gatto I, Monforte G, Passalacqua E, Antonucci V, Aricò AS. Investigation of carbon supported Pt and PtCo electrocatalysts by low-energy ion scattering and X-ray photoelectron spectroscopy: influence of the surface characteristics on performance and degradation. ECS Trans 2011;35:83–91.
[16] Teliska M, Murthi VS, Mukerjee S, Ramaker DE. Correlation of water activation, surface properties, and oxygen reduction reactivity of supported Pt-M/C bimetallic electrocatalysts using XAS. J Electrochem Soc 2005;152:A2159–69.
[17] Qian Y, Wen W, Adcock PA, Jiang Z, Hakim N, Saha MS, et al. PtM/C catalyst prepared using reverse micelle method for oxygen reduction reaction in PEM fuel cells. J Phys Chem C 2008;112:1146–57.
[18] Di Noto V, Negro E. Patent PCT/IT2009/000278, 2009.
[19] Di Noto V, Negro E. Development of nano-electrocatalysts based on carbon nitride supports for the ORR processes in PEM fuel cells. Electrochim Acta 2010;55:7564–74.
[20] Antolini E. Formation of carbon-supported PtM alloys for low temperature fuel cells: a review. Mater Chem Phys 2003;78:563–7.
[21] Di Noto V, Negro E, Gliubizzi R, Lavina S, Pace G, Gross S, et al. A Pt–Fe carbon nitride nano-electrocatalyst for polymer electrolyte membrane fuel cells and direct-methanol fuel cells: synthesis, characterization, and electrochemical studies. Adv Funct Mater 2007;17:3626–38.
[22] Di Noto V, Negro E, Gliubizzi R, Gross S, Maccato C, Pace G. Pt and Ni carbon nitride electrocatalysts for the oxygen reduction reaction. J Electrochem Soc 2007;154:B745–56.
[23] Di Noto V, Negro E. A new Pt–Rh carbon nitride electrocatalyst for the oxygen reduction reaction in polymer electrolyte membrane fuel cells: synthesis, characterization and single-cell performance. J Power Sources 2010;195:638–48.
[24] Di Noto V, Negro E, Vezzù K, Toniolo L, Pace G. Interplay between structural and electrochemical properties of Pt–Rh carbon nitride electrocatalysts for the oxygen reduction reaction. Electrochim Acta 2011;57:257–69.
[25] Di Noto V, Negro E, Polizzi S, Riello P, Atanassov P. Preparation, characterization and single-cell performance of a new class of Pd-carbon nitride electrocatalysts for oxygen reduction reaction in PEMFCs. Appl Catal B-Environ 2012;111–112:185–99.
[26] Di Noto V, Negro E. Pt–Fe and Pt–Ni carbon nitride-based "Core-Shell" ORR electrocatalysts for polymer electrolyte membrane fuel cells. Fuel Cells 2010;10:234–44.
[27] Di Noto V, Negro E, Polizzi S, Agresti F, Giffin GA. Synthesis-structure-morphology interplay of bimetallic :core- shell" carbon nitride nano-electrocatalysts. ChemSusChem 2012;5:2451–9.
[28] Di Noto V, Negro E, Polizzi S, Vezzú K, Toniolo L, Cavinato G. Synthesis, studies and fuel cell performance of "core-shell" electrocatalysts for oxygen reduction reaction based on a PtNix carbon nitride "shell" and a pyrolyzed polyketone nanoball "core". Int J Hydrogen 2014;39(6):2812–27.
[29] Platinum, #87–0647 JCPDS-ICDD. PCPDFWIN database. Version 2.1; 2000.
[30] Nickel, #87–0712 JCPDS-ICDD. PCPDFWIN database. Version 2.1; 2000.
[31] Yang H, Vogel W, Lamy C, Alonso-Vante N. Structure and electrocatalytic activity of carbon-supported Pt-Ni alloy nanoparticles toward the oxygen reduction reaction. J Phys Chem B 2004;108:11024–33.
[32] Graphite, #75–2078 JCPDS-ICDD. PCPDFWIN database. Version 2.1; 2000.
[33] Gattrell M, MacDougall B. In: Vielstich W, Lamm A, Gasteiger HA, editors. Handbook of fuel cells: fundamentals technology and applications. Chichester: John Wiley & Sons; 2003. p. 443–64.
[34] Schmidt TJ, Paulus UA, Gasteiger HA, Behm RJ. The oxygen reduction reaction on a Pt/carbon fuel cell catalyst in the presence of chloride anions. J Electroanal Chem 2001;508:41–7.
[35] Di Noto V, Negro E, Gliubizzi R, Lavina S, Pace G. New bimetallic catalysts for the oxygen reduction reaction (ORR) based on Ni and Pt carbide: synthesis, characterization and electrochemical studies. ECS Trans 2007;2:83–91.
[36] Pozio A, De Francesco M, Cemmi A, Cardellini F, Giorgi L. Comparison of high surface Pt/C catalysts by cyclic voltammetry. J Power Sources 2002;105:13–9.
[37] Koper MTM, Lai SCS, Herrero E. In: Koper MTM, editor. Fuel cell catalysis – a surface science approach. Hoboken, NJ: John Wiley & Sons; 2009. p. 159–208.
[38] Nart FC, Vielstich W. In: Vielstich W, Lamm A, Gasteiger HA, editors. Handbook of fuel cells: fundamentals technology and applications. Chichester: John Wiley & Sons; 2003. p. 302–15.
[39] Yang H, Coutanceau C, Léger J-, Alonso-Vante N, Lamy C. Methanol tolerant oxygen reduction on carbon-supported Pt–Ni alloy nanoparticles. J Electroanal Chem 2005;576:305–13.
[40] Schmidt TJ, Gasteiger HA. In: Vielstich W, Lamm A, Gasteiger HA, editors. Handbook of fuel cells: fundamentals technology and applications. Chichester: John Wiley & Sons; 2003. p. 316–33.
[41] Hammer B, Morikawa Y, Nørskov JK. CO chemisorption at metal surfaces and overlayers. Phys Rev Lett 1996;76:2141–4.
[42] Obradovic MD, Tripkovic AV, Gojkovic SL. Oxidation of carbon monoxide and formic acid on bulk and nanosized Pt–Co alloys. J Solid State Electrochem 2012;16:587–95.